

# Supplementary materials for $\ll$ Charge Number Dependence of the Dephasing Rates of a Graphene Double Quantum Dot in Circuit QED architecture $\gg$

Guang-Wei Deng,<sup>1,2</sup> Da Wei,<sup>1,2</sup> J.R. Johansson,<sup>3</sup> Miao-Lei Zhang,<sup>1,2</sup> Shu-Xiao Li,<sup>1,2</sup> Hai-Ou Li,<sup>1,2</sup> Gang Cao,<sup>1,2</sup> Ming Xiao,<sup>1,2</sup> Tao Tu,<sup>1,2</sup> Guang-Can Guo,<sup>1,2</sup> Hong-Wen Jiang,<sup>4</sup> Franco Nori,<sup>5,6</sup> and Guo-Ping Guo<sup>1,2,\*</sup>

<sup>1</sup>Key Laboratory of Quantum Information, University of Science and Technology of China, Chinese Academy of Sciences, Hefei 230026, China

<sup>2</sup>Synergetic Innovation Center of Quantum Information & Quantum Physics, University of Science and Technology of China, Hefei, Anhui 230026, China

<sup>3</sup>iTHES, RIKEN, Wako-shi, Saitama, 351-0198 Japan

<sup>4</sup>Department of Physics and Astronomy, University of California at Los Angeles, California 90095, USA

<sup>5</sup>CEMS, RIKEN, Wako-shi, Saitama, 351-0198 Japan

<sup>6</sup>Physics Department, The University of Michigan, Ann Arbor, Michigan 48109-1040, USA

## I. DEVICE AND MEASUREMENT CIRCUIT

The samples are fabricated as follows. First we mechanically exfoliated the graphene from its bulk, KISH graphite (Kyocera. Inc), to an undoped silicon chip with 285 nm oxide. Second, electron beam lithography (EBL) was employed several times, starting with the fabrication of alignment marks, then plasma-etching masks and electrode patterns. The EBL resists used were PMMA 950k A4 for the first step and double-layered PMMA 950k A2 for the latter two steps. We developed the sub-micrometer patterns under 0 to establish a better control of the device specifications. Through etching out all the undesired part of the graphene sheet to realize the designed device, we strove for the all-metal-side-gated configuration, to avoid unstable gate terminals. This etching was carried out by inductively-coupled plasma (ICP), using a 4:1 gas mixture of Oxygen to Argon. For mark-

s and electrodes we deposited 5 nm Ti and 45 nm Au with an electron-beam evaporator. Finally, the resonator was fabricated by optical lithography followed by metal deposition in a thermal evaporator. The reflection-line resonator (RLR)[1–3] consists of two coupled differential microstrip lines. A stable electromagnetic field is formed between the two microstrips when a microwave field with equal magnitude but opposite phase is applied to the resonator through the 180-degree hybrid [Fig. S1(a)] [1]. The reflected signal  $S_{11}$  is measured by a network analyzer (NA). The resonator was patterned using optical lithography with a 2  $\mu\text{m}$  thick layer of photoresist. The wafer was subsequently deposited with a 200 nm thick layer of aluminum (Al), thermally evaporated at the rate of 1  $\text{\AA}/\text{s}$ , and lifted-off in acetone. Aluminum is superconducting under about 26 mK and the internal loss of the resonator can be neglected. The amplitude and phase spectra are obtained from the NA and can be fitted with the model of a  $\lambda/2$  open-ended microstrip resonator [1], from which the resonance frequency and quality factor,  $Q$ , can be extracted. Most of our resonators have a resonance frequency near 6.3 GHz, and  $Q$  can be varied largely from several hundred up to several tens of thousands by changing the coupling capacitance. As a resonator with large  $Q$  can be used as quantum storage and one with low  $Q$  is suitable for readout, we design the coupling capacitance so that the  $Q$  is about 5000 without coupling to a quantum dot (QD). When the resonator is coupled to the double quantum dot (DQD), the  $Q$  is about 3000 for our device. This decrease of  $Q$  may be caused by current leakage through the quantum dot at the end of the resonator. Left and right plunger gates (LP and RP) are directly connected to the two striplines of the resonator. Computer simulations of this design, using the software High Frequency Structure Simulator (HFSS), show that the dc bias and ac microwave signals do not interfere, and this has also been verified experimentally in several test samples. The input and output ports of the NA are connected to the resonator via a PE-8402 circulator and a 180-degree hybrid, which direct the signal reflected by the resonator back to the NA. Furthermore, two 30 dB attenuators are connected between the NA output port and the circulator, reducing the lower limit of the power

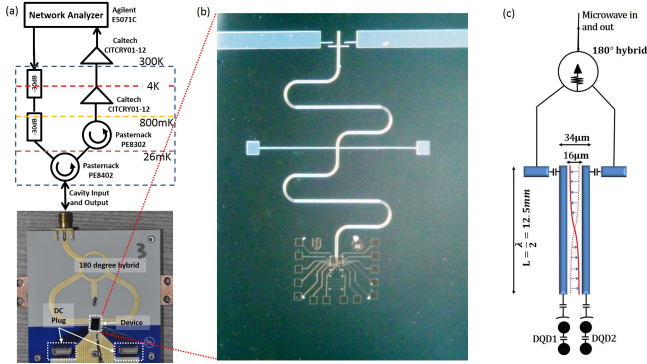


FIG. S1. **Schematic diagram of the hybrid DQD-resonator device.** (a) Schematic of the measurement setup and photograph of the high-frequency sample holder. (b) Photograph of the reflection-line-resonator. (c) Schematic of the measured device, the scale bars are used for resonator only (not for the DQDs).

\* Corresponding author: gpguo@ustc.edu.cn

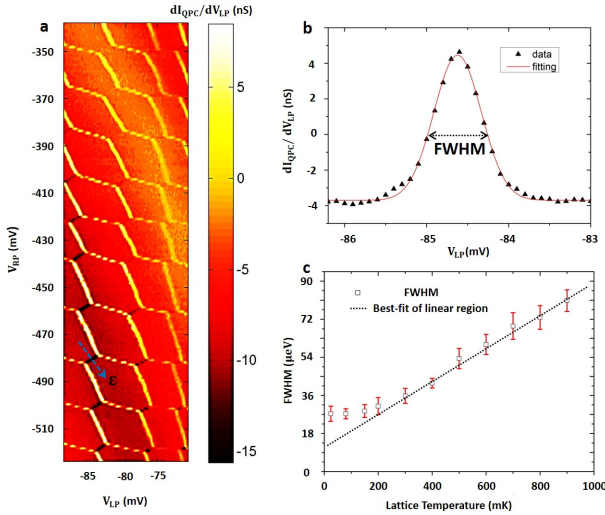


FIG. S2. **Temperature dependence measurement.** (a) The charge-stability diagram of the graphene DQD, obtained using a QPC charge-sensing measurement at the base temperature. (b) The full width at half maximum (FWHM) of the QPC signal as a function of  $\epsilon$ . The FWHM is extracted from the data using a Lorentzian fit. The temperature is varied from the base temperature up to 1 K, and here we show the result at the base temperature. (c) The FWHM as a function of the lattice temperature. The dashed line is the best linear fit for the high temperature region.

applied to the resonator to -130 dBm. The reflected signal is amplified at 4 K and at room temperature, and an isolator is used to prevent noise from the amplifiers and the environment from reaching the sample.

## II. MEASUREMENTS OF THE GRAPHENE QUANTUM DOT

Using a QPC we were able to perform charge-sensing measurements and obtained the charge-stability diagram of the device, typical result of a DQD is shown in Fig. S2. In order to prevent the microwave power from being absorbed by the substrate, we choose undoped silicon with a 300 nm thermal oxide as substrate. The back gate is grounded during the measurement. For varying lattice temperature, we measured the full width at half maximum (FWHM) of the QPC signal as a function of  $\epsilon$ .

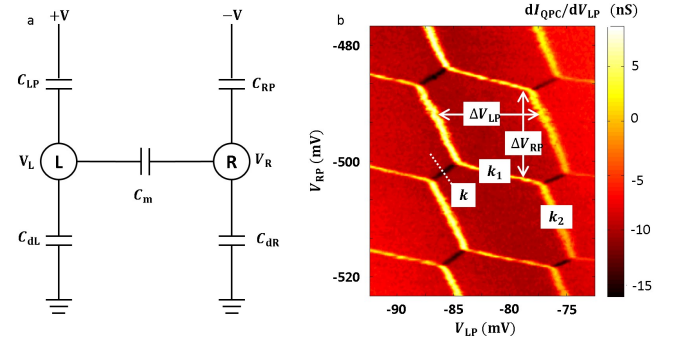


FIG. S3. **Capacitance model for the hybrid system.** (a) Equivalent circuit diagram of the hybrid system.  $+V$  and  $-V$  represent the equivalent voltage produced by the microwave from the two strips of RLR.  $C_{LP}$  is the coupling capacitance between the LP gate and the left dot, and similarly for  $C_{RP}$ .  $C_m$  is the capacitance between the two dots.  $C_{dL}$  is the total capacitance of left dot except  $C_{gL}$  and  $C_m$ , also similarly for  $C_{dR}$ .  $V_L$  and  $V_R$  are the effective voltages induced by  $+V$  and  $-V$ . (b) A typical charge stability diagram and definition of specify parameters.

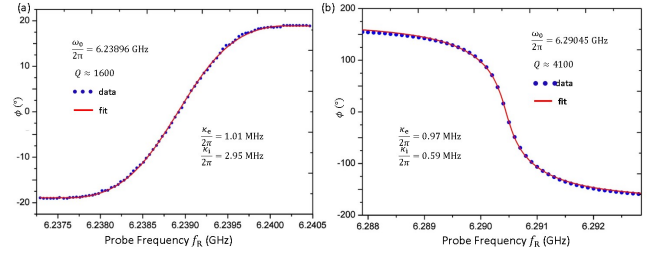


FIG. S4. **Phase responses.** The phase response of the resonator as a function of the applied microwave frequency, together with a theoretical fit. Here we show results for the two cases of  $\kappa_e < \kappa_i$  (a) and  $\kappa_e > \kappa_i$  (b), corresponding to two typical resonators. The phase response as a function of probe frequency have different shapes depending on whether the internal or external dissipation dominates.

Here  $2t_C$ ,  $T_e$ , and the FWHM are related as [4] :

$$\frac{\tanh(\delta)}{2\delta} = \frac{\delta^2}{(\sqrt{\delta^2 + F^2})^3} \tanh(\sqrt{\delta^2 + F^2}) + \frac{F^2}{(\delta^2 + F^2)} \coth^{-2}(\sqrt{\delta^2 + F^2}), \quad (1)$$

$$F = \frac{\text{FWHM}(eV)}{2} \frac{1}{2k_B T_e},$$

$$\delta = \frac{2t_C}{2k_B T_e},$$

where  $k_B$  is the Boltzmann constant,  $T_e$  is the electron temperature and  $\text{FWHM}(eV)$  is the FWHM in energy unit, which can be transformed from the gate voltage by the plunger gate lever arm. Lever arm is defined as  $\alpha_L = C_{LP}/C_L$ , where  $C_L$  is the total capacitance of the

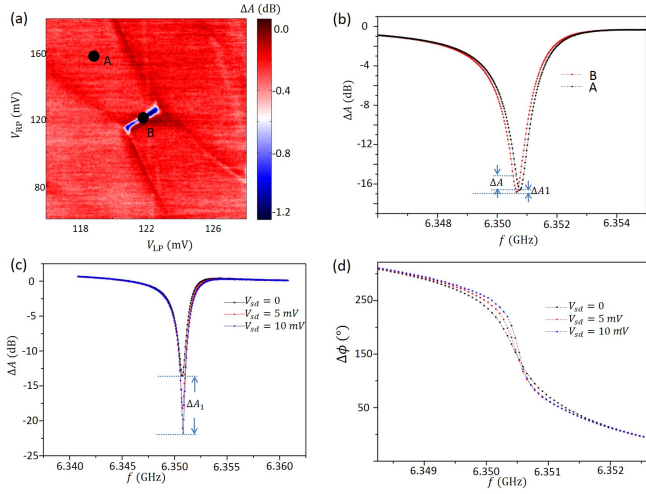


FIG. S5. **Resonator responses under different DQD conditions.** (a) Typical DQD charge stability diagram. (b) Amplitude response as a function of driving frequency for two points denoted in (a).  $\Delta A$  is the measured amplitude change when fixing the probe frequency at 6.35086 GHz and  $\Delta A_1$  is caused by the addition of dissipation. Amplitude (c) and phase (d) responses for different DQD bias voltages. The large  $\Delta A_1$  means that the dissipation is the main effect in large bias condition.

left dot (the definition of the capacitance can be seen in Fig. S3), and the same with  $\alpha_R$ .

By fitting the FWHM as a function of temperature, we extract  $2t_C$ ,  $T_e$ , and the lever arm  $\alpha$  of the plunger gates. Here different values of  $2t_C$  can be obtained at different interdot charge transition states as it cannot be tuned in-situ,  $T_e$  is about 150 mK in our device, and the lever arm is about 6%.

### III. CAPACITANCE MODEL FOR THE HYBRID SYSTEM

The coupling between the graphene DQD and the RLR can be described by an equivalent circuit, shown in Fig. S3(a). We define

$$\nu = \frac{V_L - V_R}{+V - (-V)} = \frac{V_L - V_R}{2V}, \quad (2)$$

where  $\nu$  can be understood as the lever arm between microwave energy in RLR and the graphene DQD. The coupling strength is then given by  $g_C = \omega_0 \nu \sqrt{\frac{2Z_0}{R_Q}}$  [5], where  $R_Q \approx 26 \text{ k}\Omega$  is the quantum resistance and  $Z_0 = 50 \Omega$  is the characteristic impedance. By simple circuit analysis and the constant interaction model [6], we obtain

$$\nu = \frac{\alpha_L + \alpha_R + \alpha_R \frac{\Delta V_{LP}}{\Delta V_{RP}} k_1 + \alpha_L \frac{\Delta V_{RP}}{\Delta V_{LP}} \frac{1}{k_2}}{1 - \frac{k_1}{k_2}} \quad (3)$$

The slopes  $k_1$ ,  $k_2$  and  $V_{LP}$ ,  $V_{RP}$  are shown in Fig. S3. For the interdot transition line near the region  $V_{LP} = 310 \text{ mV}$ ,  $V_{RP} = 220 \text{ mV}$ , we calculate  $g_C$  to be about 12 MHz. This coupling strength is comparable to the previously reported values for semiconductor QDs coupled to TLR [7, 8]. With  $\hbar g_C = Ed$ , and the photon-induced electric field  $E$  of the order of  $10^{-1} \text{ V/m}$ , we estimate that the dipole moment of the DQD system is of the order of  $d = 1000 e a_0$ , where  $a_0$  is the Bohr radius.

### IV. QUANTUM MODEL

The double quantum dot can be modeled as a quantum two-level system that couples to the resonator via a dipole interaction, described by the hamiltonian [9]

$$H = \hbar \Delta_0 a^\dagger a + \frac{1}{2} \hbar \Delta \sigma_z + \hbar g_{\text{eff}} (\sigma_+ a + \sigma_- a^\dagger), \quad (4)$$

which is written in the qubit eigenbasis and in the rotating-frame with respect to the probe frequency  $\omega_R$  and under the rotating wave approximation. Here  $g_{\text{eff}} = g_C \frac{2t_C}{\Omega}$ ,  $\Delta_0 = \omega_0 - \omega_R$ ,  $\Delta = \Omega - \omega_R$ ,  $\omega_0$  is the resonance frequency of the resonator,  $\Omega = \sqrt{(2t_C)^2 + \epsilon^2}$ ,  $\Omega_\pm = \pm \Omega/2$  are the eigenenergies of the quantum dot two level system. Here  $\sigma_z$  is the standard Pauli  $z$ -operator,  $\sigma_-$  ( $\sigma_+$ ) and  $a$  ( $a^\dagger$ ) are the annihilation (creation) operators for the quantum dot and resonator photons, respectively. To model the internal  $\kappa_i$  and external  $\kappa_e$  dissipation rates of the resonator, and the qubit relaxation rate  $\gamma_1$  and dephasing rate  $\gamma_2$ , we first consider the Lindblad master equation

$$\dot{\rho} = -i[H, \rho] + \kappa \mathcal{D}[a]\rho + \gamma_1 \mathcal{D}[\sigma_-]\rho + \frac{1}{2} \gamma_2 \mathcal{D}[\sigma_z]\rho, \quad (5)$$

where  $\mathcal{D}[a]\rho = a\rho a^\dagger - \frac{1}{2}a^\dagger a\rho - \frac{1}{2}\rho a^\dagger a$  is the Lindblad dissipator. We then include the input-output theory [10], where  $\kappa = \kappa_e + \kappa_i$  is the total dissipation rate of the resonator. The corresponding Heisenberg-Langevin equations of motion for the operators  $a$ ,  $\sigma_-$  and  $\sigma_z$  are

$$\dot{a} = -i\Delta_0 a - ig_{\text{eff}}\sigma_- - \frac{1}{2}\kappa a + \sqrt{\kappa_e}a_{\text{in}}, \quad (6)$$

$$\dot{\sigma}_- = -i\Delta\sigma_- + ig_{\text{eff}}a\sigma_z - \frac{1}{2}\gamma_1\sigma_- - \gamma_2\sigma_-, \quad (7)$$

where we have neglected the quantum noise terms for the quantum dot operators. For simplicity, we will also assume that the quantum dot remains in its ground state [11, 12],  $\sigma_z \rightarrow -1$ . The boundary condition from the coupling of the external transmission line to our single-sided resonator is  $a_{\text{in}} + a_{\text{out}} = \sqrt{\kappa_e}a$ . Combining these results we finally obtain the reflection coefficient

$$S_{11} = \frac{a_{\text{out}}}{a_{\text{in}}} = -\frac{i(\omega_0 - \omega) + g_{\text{eff}}\chi + \frac{\kappa_i - \kappa_e}{2}}{i(\omega_0 - \omega) + g_{\text{eff}}\chi + \frac{\kappa_i + \kappa_e}{2}}, \quad (8)$$

$$\chi = \frac{g_{\text{eff}}}{i(\Omega - \omega) + \frac{1}{2}\gamma_1 + \gamma_2}. \quad (9)$$

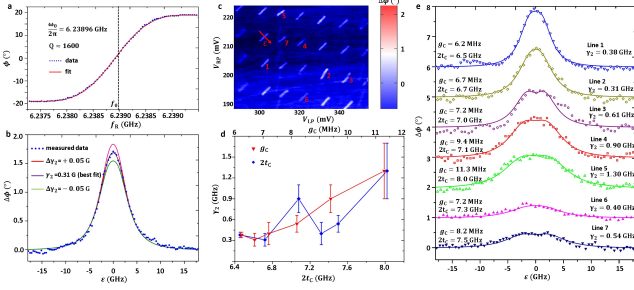


FIG. S6. **Parameter extraction.** (a) Best fit of the phase versus frequency curve. Quality factor and resonance center can be obtained. (b)  $\gamma_2$  sensitivity of the fit. The purple line is the best fit curve of the experimental data (blue dots). To slightly increase/decrease the  $\gamma_2$  by 0.05 GHz from its best fit value, the red and green lines, then, show obvious deviation from the data, suggesting that such fit-obtained  $\gamma_2$  value is of high accuracy. (c) A typical charge stability diagram of the graphene DQD, where the interdot transition lines are labeled from 1 to 7 in corresponding with the marked data in (e). (d)  $\gamma_2$  dependence of  $2t_C$  (blue) and  $g_C$  (red). (e) Experimental data of the phase shift  $\Delta\phi$ , as a function of the DQD detuning  $\epsilon$ , collected from different interdot transition lines as shown in (c). Each measurement is taken at a fixed probe frequency  $f_R$ , which is close to the cavity resonance frequency  $f_0$ . The theoretical model used in the fitting is described in the supplementary materials. The free fitting parameters were  $2t_C$ ,  $g_C$  and  $\gamma_2$ , while other DQD and resonator parameters were assumed to be known from other measurements and calibrations.

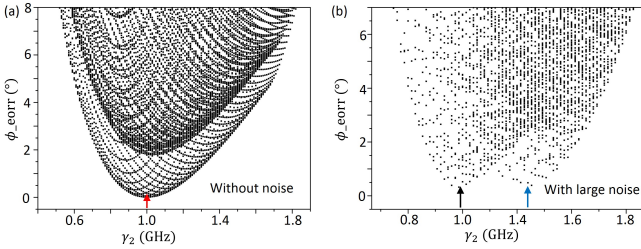


FIG. S7. **Simulation of the fitting procedure.** (a)  $\phi_{error}$  as a function of  $\gamma_2$  for a giving curve without noise. Here  $\gamma_2$ ,  $2t_C$ , and  $g_C$  are ergodic values in giving intervals. (b)  $\phi_{error}$  as a function of  $\gamma_2$  with a 0.5 degree Gaussian type noise.

## V. FITTING THE FREE PARAMETERS

Figure S4 shows the phase response as a function of probe frequency and the best fit for two typical resonators with  $\kappa_e < \kappa_i$  and  $\kappa_e > \kappa_i$ , respectively. After obtaining the parameters  $\omega_0$ ,  $\kappa_i$ , and  $\kappa_e$ , we can extract the remaining parameters  $g_C$ ,  $2t_C$ , and  $\gamma_2$  by further fitting  $\Delta\phi$  as a function of  $\epsilon$  with a least-square method. The parameters except  $\gamma_2$  can be extracted independently:  $2t_C$  can be obtained by a temperature dependence measurement,  $g_C$  can be obtained by a capacitive model, where

$g_C = \omega_0 \nu \sqrt{2Z_0/R_Q}$ . Here  $R_Q \approx 26K\Omega$  is the quantum resistance and  $Z_0 = 50\Omega$  is the characteristic,  $\nu$  is the lever arm between microwave energy in RLR and the DQD. Here in our fitting, the dissipation is neglected because the dissipation is much smaller than the dispersive effect in our experiment [see Fig. S5(b)]. Dissipation increases obviously when the DQD bias increases [13] [see Fig. S5(c,d)]. Figure S6 shows the fitting results of a typical sample in our experiment, where 7 charge states are included. Figure S6(e) indicates perfect fit of each points. When we used the fitting procedures, we have made following simulations to test the reliability of the fitting method: First, we compare the  $g_C$  and  $2t_C$  fitted from individual fitting procedure and fitting with  $g_C$ ,  $2t_C$  and  $\gamma_2$  all three as free parameters, finding that the values obtained from the two method can be in consistence with each other [14]. Second, after the fitting with  $g_C$ ,  $2t_C$  and  $\gamma_2$  all three as free parameters, we replace one of the parameters by another value, for example  $2t_C$ , and refit with the other two as free parameters. The least-square method cannot fit the curve very well, which indicates that the three parameters contribute to different parts of the curve and the variation will not be absorbed by the other. Third, to further test whether the variation will be absorbed by one of the other parameters, we use a simulation as following. Starting from a giving theoretical curve  $\phi_0 = \phi(\gamma_2 = 1GHz, 2t_C = 6.3GHz, g_C = 15MHz)$ , we define  $\phi_{error} = \phi(\gamma_2, 2t_C, g_C) - \phi_0$ , where  $\gamma_2$ ,  $2t_C$ , and  $g_C$  can be ergodic values in giving intervals. The fitting procedure is equivalent to finding a smallest  $\phi_{error}$ . Of cause the curve will be convergent to  $\phi_0$ . We show  $\phi_{error}$  as a function of  $\gamma_2$  in Fig. S7. The discrete curves in Fig. S7(a) indicate a fixed wrong  $2t_C$ , and  $g_C$  will lead to a wrong  $\gamma_2$ . The variation of  $2t_C$ , and  $g_C$  cannot be compensated by  $\gamma_2$ , in other words, the variation will not be absorbed by one of the other parameters. However, for large noise system, the case is more complicated. We mode the noise by applying a Gaussian type noise to the theoretical curve  $\phi_0 = \phi(\gamma_2 = 1G, 2t_C = 6.3G, g_C = 15M)$ , we find for small noise case, the curve will be convergent to the right value. However, if the phase noise is very large, the curve ( $\phi_{error}$ ) will convergent to two different values (Fig. S7(b) is obtained by a phase noise of 0.5 degree). In our fitting procedure, we used several times average to decrease the noise, the measured phase noise in our system is below 0.1 degree. For this order of noise, the curve is hardly to be convergent to two values, in our many times simulation. For the above three reasons, we are confident that our fitting procedure is accurate.

## VI. INTERDOT TUNNELING RATES AND CHARGING ENERGY DEPENDENCE

Figure S8 shows the interdot tunneling rates depend on the charge number in the right dot of device A, corresponding one-to-one with Fig. 3(c) in the main text. The value of  $2t_C$  in our device is around 6-8 GHz. Fig-

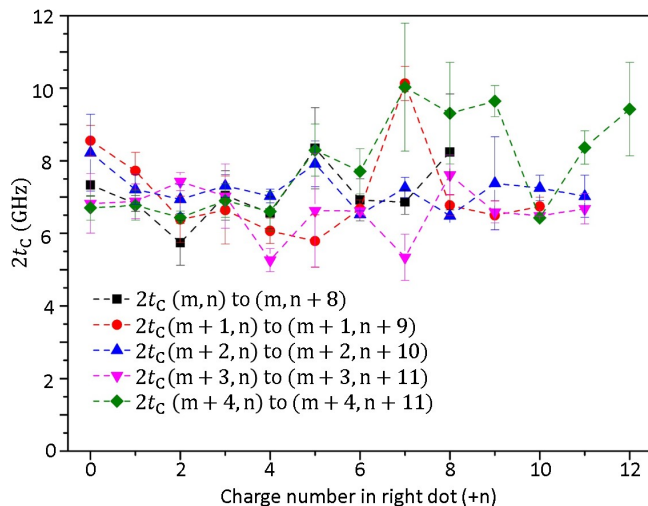


FIG. S8. **Interdot tunneling rates dependence.** Interdot tunneling rates as functions of the charge number in the right dot, where five columns are studied, which has a one-to-one correspondence with Fig. 3(c) in the main text.

ure S6(c) shows the charging energy  $E_C$  dependence of the charge number in the right dot. Four-fold degeneracy manifested in  $E_C$  [15] is not observed in our device. Here

$E_C$  is measured by the Coulomb diamond of the right dot [see Fig. S9(b)], corresponding to the four-fold periodicity in the dephasing rates [see Fig. S9(a)]. Charge number dependence in the left dot is shown in Fig. S9(d); however, the well-shaped honeycomb cells are only 5, and a reliable conclusion is difficult to reach.

## VII. CHARGE NUMBER DEPENDENCE OF DEVICE B AND C

Figure S10 shows the charge number dependence of the dephasing rate in device B and C. We studied  $3 \times 10$  ordered cells in device B and two periodicity in the dephasing rate depend on charge number in one dot was found [Fig. S10(a,b)]. However, only  $3 \times 6$  ordered cells were found in device C and one periodicity was studied [Fig. S10(c,d)]. The reason why we cannot find a very large ordered cells may be due to the puddle and edge states. The ordered cells show similar periodicity with device A shown in the main text, proving this spin and valley degree induced periodicity is not sample dependent.

To be noted, a large portion of the materials, presented in the first three sections, regarding the measurement and circuit analysis details of the hybrid system, come from our previous preprint [16].

- 
- [1] D. Pozar, *Microwave Engineering* (Wiley, 2004).
  - [2] V. E. Manucharyan, J. Koch, L. I. Glazman, and M. H. Devoret, *Science* **326**, 113 (2009).
  - [3] M.-L. Zhang, G.-W. Deng, S.-X. Li, H.-O. Li, G. Cao, T. Tu, M. Xiao, G.-C. Guo, H.-W. Jiang, S. I., and G.-P. Guo, *Appl. Phys. Lett.* **104**, 083511 (2014).
  - [4] D. Wei et al., *Sci. Rep.* **3**, 3175 (2013).
  - [5] L. Childress, A. Sorensen, and M. Lukin, *Phys. Rev. A* **69**, 042302 (2004).
  - [6] W. G. van der Wiel, S. De Franceschi, J. M. Elzerman, T. Fujisawa, S. Tarucha, and L. P. Kouwenhoven, *Rev. Mod. Phys.* **75**, 1 (2002).
  - [7] T. Frey, P. J. Leek, M. Beck, A. Blais, T. Ihn, K. Ensslin, and A. Wallraff, *Phys. Rev. Lett.* **108**, 046807 (2012).
  - [8] H. Toida, T. Nakajima, and S. Komiyama, *Phys. Rev. Lett.* **110**, 066802 (2013).
  - [9] K. D. Petersson, L. W. McFaul, M. D. Schroer, M. Jung, J. M. Taylor, A. A. Houck, and J. R. Petta, *Nature* **490**, 380 (2012).
  - [10] M. J. Collett and C. W. Gardiner, *Phys. Rev. A* **30**, 1386 (1984).
  - [11] D. W. Vernooy and H. J. Kimble, *Phys. Rev. A* **56**, 4287 (1997).
  - [12] H. J. Carmichael, *Phys. Rev. Lett.* **55**, 2790 (1985).
  - [13] S. Marco and L. H. Karyn, *Phys. Rev. B* **89**, 195127 (2014).
  - [14] T. Frey et al., *Phys. Rev. B* **86**, 115303 (2012).
  - [15] W.-J. Liang, M. Bockrath, and H. Park, *Phys. Rev. Lett.* **88**, 126801 (2002).
  - [16] G.-W. Deng et al., arXiv: 1310.6118 (2013).

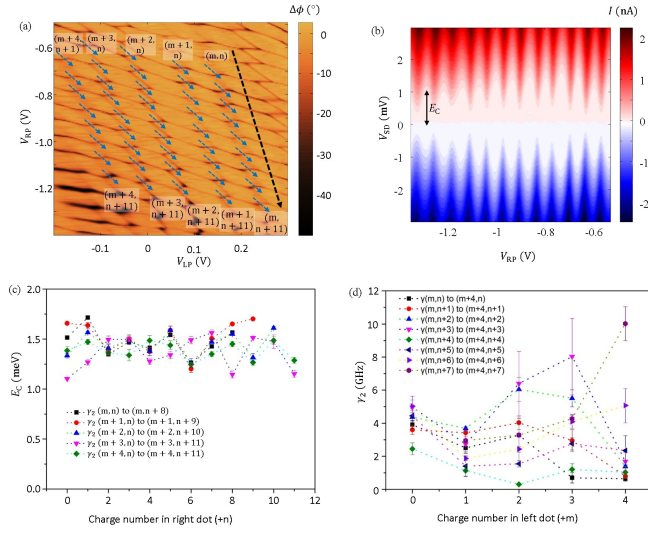


FIG. S9. **Charging energy dependence of device A.** (a) Charge stability diagram of the DQD, which is the same as Fig. 3(b) in the main text. (b) Coulomb diamond diagram of the right dot. It was obtained along the dashed black line in (a), while the horizontal axis only denotes the RP gate voltage. The charging energy of an addition electron can be obtained from the diamond size, shown by the solid arrow. (c) Charging energy  $E_C$  as a function of charge number in the right dot, where five columns are studied, which has a one-to-one correspondence with Fig. 3(c) in the main text. (d) Dephasing rates as a function of electron number in the left dot. The data is the same as in Fig. 3(c) in the main text, but are here shown as a function of the left dot charge number.

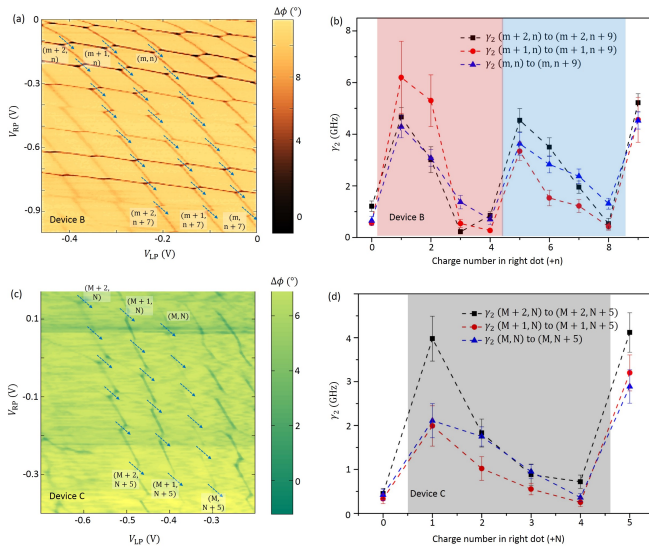


FIG. S10. **Dephasing rate dependence of device B and C.** (a) Charge stability diagram of device B. Here  $3 \times 10$  ordered cells are studied (8 rows are shown in this diagram). (b) The dephasing rates as a function of hole number in the right dot for 12 consecutive holes (from  $n$  to  $n+9$ ), which are denoted in (a). Three columns (from  $m$  to  $m+2$ ) are studied. To assist readers, the approximate periodicity has been guided by different background colors. (c) Charge stability diagram of device C, where  $3 \times 6$  ordered cells are studied. (d) Dephasing rate dependence of device C.